Rupture energetics in crustal rock from laboratory-scale seismic tomography

Franciscus M. Aben[1], Nicolas Brantut[1], Thomas M. Mitchell[1], and Emmanuel C. David[1]

The energy released during earthquake rupture is partly radiated as seismic waves, and mostly dissipated by frictional heating on the fault interface and by off-fault fracturing of surrounding host rock. Quantification of these individual components is crucial to understand the physics of rupture. We use a quasi-static rock fracture experiment combined with a novel seismic tomography method to quantify the contribution of off-fault fracturing to the energy budget of a rupture, and find that this contribution is around 3% of the total energy budget, and 10% of the fracture energy G_c. The off-fault dissipated energy changes the physical properties of the rock at the early stages of rupture, illustrated by the 50% drop in elastic moduli of the rock near the fault, and thus is expected to greatly influence later stages of rupture and slip. These constraints are a unique benchmark for calibration of dynamic rupture models.

1. Introduction

Strain energy released during earthquakes is partly radiated as seismic waves that cause ground shaking, and mostly dissipated by frictional heating on the fault interface and by fracturing of the rocks surrounding the fault. The latter energy sink, and a component of frictional heating, constitute the fracture energy (G_c, sometimes referred to as rupture energy) that dictates the dynamics of rupture propagation [*Rice*, 1980]. Quantification of these individual components is crucial to understand the physics of rupture, to better understand the feedback between rupture and slip processes, and to improve ground motion predictions.

Fracture energy is the work associated with the breakdown of the rock strength towards its residual frictional strength. G_c is a collective term for several dissipative processes in the breakdown zone around the rupture tip, both on and off fault [*Kanamori and Rivera*, 2006]. These dissipative processes may include shear heating, plastic yielding, on- and off-fault creation of fractures (surface energy), and grain comminution. A measure of G_c can be inferred from earthquake data [*Tinti et al.*, 2005], and from laboratory mechanical [*Wong*, 1982, 1986; *Nielsen et al.*, 2016] and acoustic data [*Lockner et al.*, 1991], but such data do not provide a breakdown of the individual components of G_c. Cumulated surface energy measured on fault rocks [*Wilson et al.*, 2005; *Chester et al.*, 2005; *Rockwell et al.*, 2009; *Faulkner et al.*, 2011; *Savage and Brodsky*, 2011] provide on- and off-fault components of G_c, but these estimates are measured on rocks that have recorded numerous earthquakes and deformation episodes and therefore do not represent a single earthquake, nor can they constrain energy dissipation into heat. Cumulated surface energy obtained from microstructural studies on off-fault damage in laboratory samples [*Moore and Lockner*, 1995; *Zang et al.*, 2000] are only static snapshots of the dynamic breakdown process. To establish the off-fault energy dissipation component G_{off}, one possibility is to use the change in off-fault elastic properties caused by off-fault deformation. Such changes must be measured *in situ* during rupture, ideally under realistic crustal conditions (i.e., at elevated pressure and temperature). This may be done by the acquisition of active seismic surveys during laboratory rupture experiments [*Lockner et al.*, 1977]. Yet, the size and geometry of the off-fault damage zone and the actual local wavespeeds therein remain unconstrained because of the lack of spatial resolution of conventional laboratory ultrasonic measurements.

Here, we combine stress, strain, and acoustic emission (AE) and ultrasonic velocity measurements obtained *in situ* during a laboratory rock fracture experiment. From this, we determine the time-resolved 3D seismic velocity structure of a growing fault zone that provides the size and geometry of the off-fault elastic properties. Taken together, our measurements allows us to estimate the partitioning of G_c into off-fault (G_{off}) and on-fault energy dissipation.

2. Method

We performed a triaxial rupture experiment on a 40 mm diameter, 100 mm length sample of dry Lanhélin granite (Brittany, France). The sample was placed into a rubber jacket equipped with 16 piezoelectric P-wave transducers, and two pairs of axial-radial strain gauges (Fig. 1). Acoustic signals were recorded by a digital oscilloscope at a 50 MHz sampling frequency, after being amplified to 40 dB. Active ultrasonic velocity surveys were performed every 5 minutes by sending a 1 MHz pulse at a voltage of 250 V to one transducer, while the other transducers recorded the resulting waveforms. During one survey, all 16 transducers were used as a source, and the results of six pulses for each source transducer were stacked to enhance the signal-to-noise ratio. In between the acoustic velocity surveys, the waveforms of acoustic emissions were recorded provided that a signal amplitude of 250 mV was surpassed on at least two transducers. All waveforms, both of active acoustic velocity surveys and AEs, consisted of 4096 datapoints (82 μs length).

The jacketed sample was placed into a triaxial deformation rig and pressurised to 100 MPa confining pressure. Axial stress was measured by a load cell, axial shortening was measured by a pair of Linear Variable Differential Transducers (LVDTs). The axial deformation was then applied by a piston that moved with a strain rate of 10^{-5} s^{-1} for the elastic portion of the stress-strain curve, and 10^{-6} s^{-1} for the remainder of the experiment. The axial shortening rate was controlled in such a way as to hamper the dynamic propagation of shear rupture, using a technique similar to that of *Lockner et al.* [1991]: The AE-rate was monitored visually and, when the AE-rate showed acceleration (about 8 hits or more per second, recorded on at least two channels), the direction of movement of the piston was reversed to reduce the load. More than 100 of such load reductions were performed. The overall fracture propagation across the sample occurred over a time interval of around 16 hours.

From the ultrasonic dataset, we computed the AE source locations together with the evolution of the seismic velocity structure within the sample by using the 3D seismic tomography code *FaATSO*, specifically designed for laboratory rock deformation experiments [*Brantut*, 2018]. 12000 of the highest quality AE events

[1]Department of Earth Sciences, University College London, London, UK

This version is a home made pdf generated from the orginal LaTeXfiles, and the formatting and editing differs from the version published by AGU. Minor differences with the official version may subsist (British spelling, figure numbering).

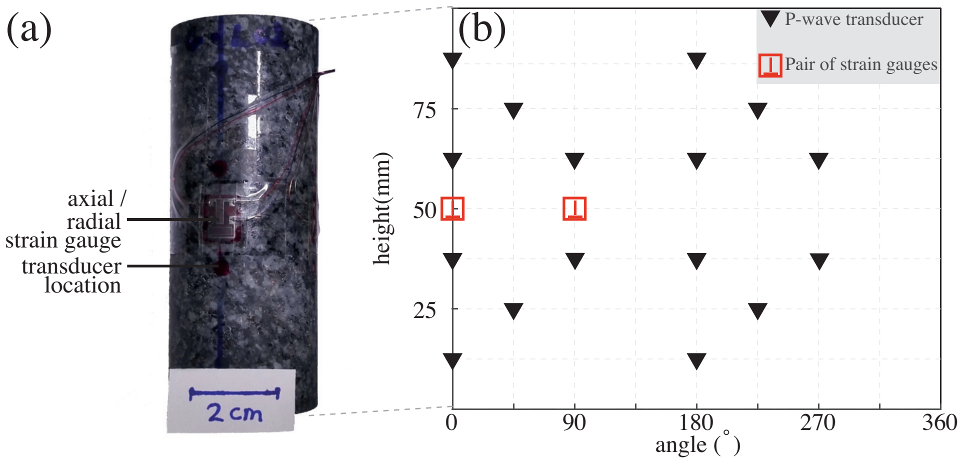

Figure 1: Sensor setup around sample. (a): Lanhélin granite sample equipped with a pair of axial/radial strain gauges. (b): Map of the distribution of the piezoelectric P-wave transducers and the strain gauges around the sample.

Table 1: Table 1: The inversion parameters used for the controlled rupture experiment.

Standard deviations (σ):	
Survey arrival time	1 μs
Anisotropy parameter	0.01 μs
a priori velocity model	0.02 log(m/s)
AE arrival time	2 μs
AE location	2 mm
AE origin time	2 μs
Correlation length	25 mm

were considered for the tomography. For all these AE events, the first *P*-wave arrivals were picked using an automated picking algorithm. The automated picks were manually checked and where necessary improved or cancelled. The acoustic data was split into 38 time intervals of 100-400 AEs that cover a more or less equidistant interval of the stress-strain curve (Fig. 2). The mean posterior model determined by FaATSO yielded the V_P structure during each time interval. The spatial resolution of the velocity structure is 5 mm, which is similar to the wavelength of the 1 MHz surveys. The velocity structure of the previous time interval was used as the *a priori* velocity structure for the next time interval. For the *a priori* velocity structure of the first time interval, we took a transverse isotropic structure derived from the first active ultrasonic surveys. The inverse problem was constrained by several inversion parameters that ascribe Gaussian variances to the input data, expressed as standard deviations (Table 1). The velocity model was ascribed a covariance as function of the variance of the velocity and a correlation length. Heterogeneities and velocity contrasts smaller than the correlation length are suppressed and smoothed, eliminating unrealistic sharp velocity contrast from the results. Such a covariance was ascribed to the anisotropy structure as well.

The AE source locations were recomputed by using the 3D seismic velocity structure from *FaATSO*. An approximation of the position of the rupture front and the seismically active fault surface for each time interval were obtained from the relocalised AE locations (Fig. S1, Text S1).

3. Results

Before the peak stress and the onset faulting, we observe an overall decrease in V_P from around 6 km/s down to 5 km/s (Fig. 2a). Then, rupture starts at the bottom of the sample and propagates upwards (Fig. S1, Movie S1). A low velocity zone develops parallel to the rupture plane and migrates along with the growing fault (delineated by the AE source locations, Fig. 2b,c and Fig. S1). Velocities in the localised zone are as low as 4.6 km/s – a 25% drop relative to the areas outside of the fault zone where V_P remains nearly constant (Fig. 2c). This corresponds to a drop of around 50% in *P*-wave modulus. We interpret this low velocity zone as the fault damage zone, which is generated ahead and along the propagating rupture tip. In the wake of the rupture tip the damage zone width decreases slightly by several millimeters. There is a widespread partial recovery of V_P throughout the damage zone (the minimum value rising from 4.6 km/s to about 4.7 km/s) at the onset of the frictional sliding stage (Fig. 2d). The V_P anisotropy at the peak stress is 13% (i.e., vertical V_P is 13% higher than horizontal V_P, Fig. S3), and increases during fault growth up to 20% in two large zones adjacent to the fault. In the wake of the passing fault tip, the change in velocity anisotropy is much less than the change in velocity (Fig. 1). The anisotropy decreases again as the axial stress is reduced during the frictional sliding stage.

The robustness of the tomographic inversion results is demonstrated by the mean posterior velocity and 500 individual posterior solutions along a fault-perpendicular transect (Fig. 3a-d). The individual solutions (grey curves) show how the V_P along the transect evolves from a near-constant value (Fig. 3a) to a localised reduction in V_P as the rupture tip approaches (Fig. 3b), which is amplified once the rupture tip has passed the transect (Fig. 3c). Again, the P-wave velocity increases slightly at the frictional sliding stage (Fig. 3d). A single solution tomography slice (Fig. 3e) shows the same features as the (interpolated) mean solution (Fig. 2).

4. Rupture energetics

Now, we can determine the fracture energy G_c, the total dissipated energy, and the off-fault dissipated energy G_{off}. G_c and the total dissipated energy are computed from the shear stress vs. fault slip record[*Wong*, 1982] up to the slip-weakening distance δ_0 (Fig. 4). We assume that all axial shortening is caused by slip along the fault from localisation onward. Axial shortening is corrected for elastic strain by using the intact elastic moduli for the rock. G_c is 2.7×10^4 Jm^{-2}, similar to previous experimental results ($1.3 - 2.9 \times 10^4$ Jm^{-2}) [*Wong*, 1982, 1986; *Lockner et al.*, 1991].

Next, we estimate the off-fault dissipated energy G_{off} during the slip-weakening stage. G_{off} is given by the change in stored elastic strain energy (i.e. elastic softening) around the fault interface. These elastic compliance changes are caused by off-fault dissipative processes, of which microcracking is dominant. Strain derived

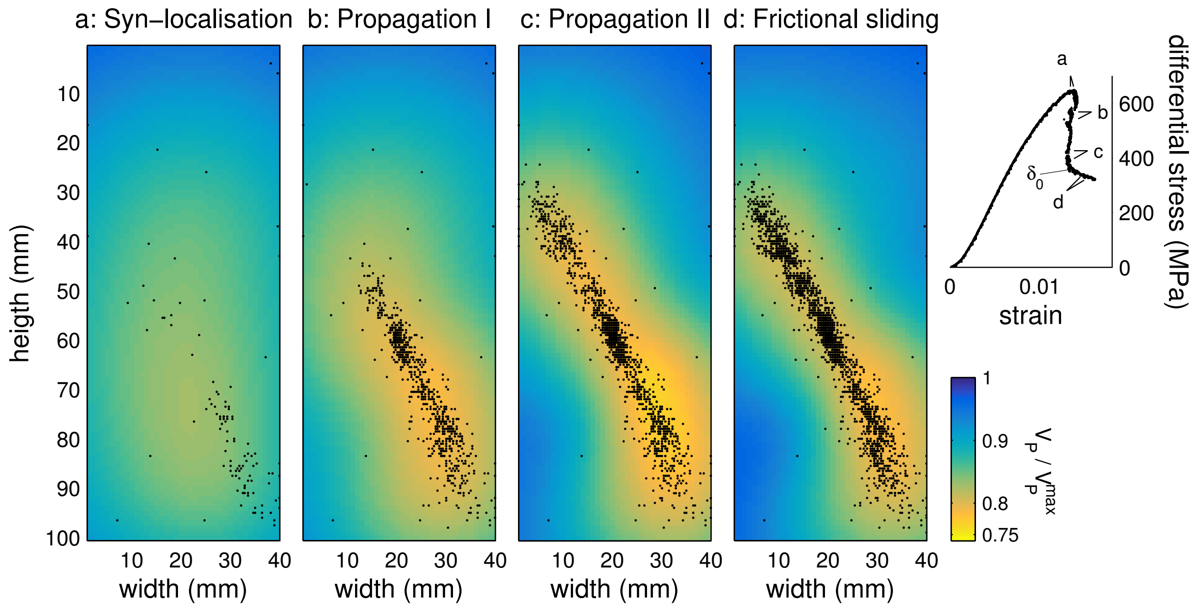

Figure 2: Tomographic slices of the horizontal V_P normalised to the initial velocity. The slices run through the centre of the sample, perpendicular to the rupture. The four slices represent time intervals (a) during localization of deformation, (b, c) during two stages of rupture propagation, and (d) during frictional sliding of the fault. The corresponding parts of the stress-strain curve are indicated on the right. δ_0 indicates the slip-weakening distance. All AE source locations up to the time interval are projected onto the slice, illustrating the rupture propagation. The AE source locations are within 2.5 mm distance perpendicular to the slide, and were determined using the 3D seismic velocity model. The seismic velocities are smoothed to a 1 mm resolution. See movie S1 for the complete evolving seismic structure.

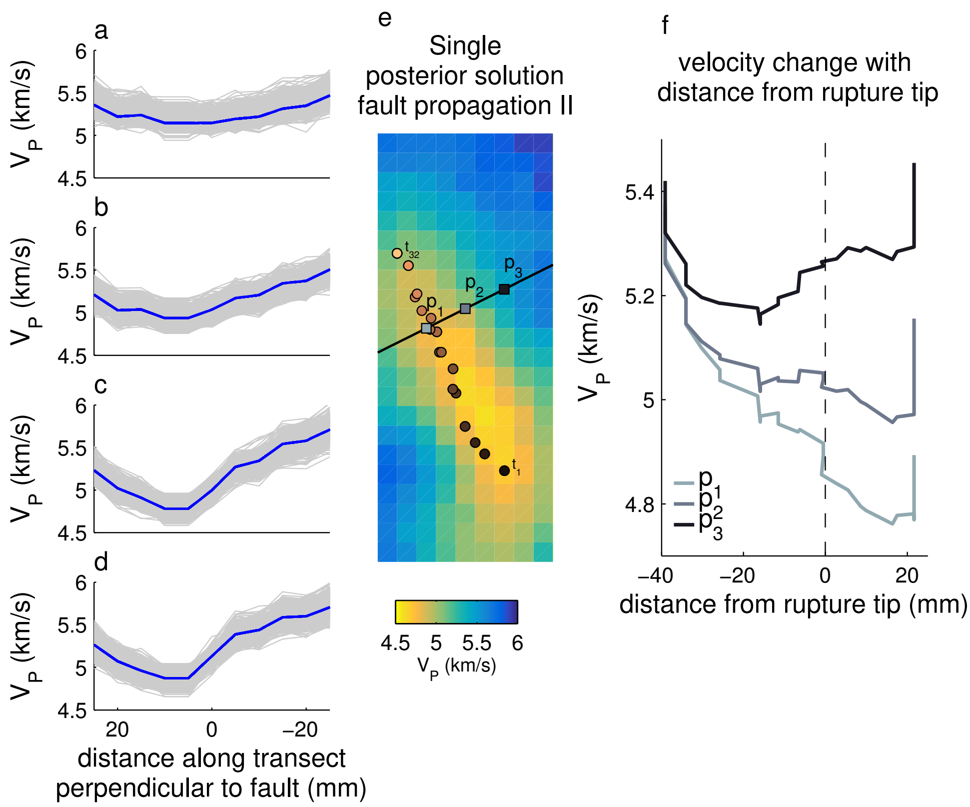

Figure 3: Posterior solutions and V_P evolution with respect to the rupture tip position (a-d): The V_P of 500 individual posterior solutions (gray curves) and the V_P of the mean posterior solution (blue curve) along a fault-perpendicular transect, for the time intervals shown in Fig. 2. (e): An individual posterior solution (spatial resolution 5 mm) shows a similar velocity structure as the mean solutions in Fig. 2c. The black line indicates the location of the transect in (a-d) and the squares indicate points p_1-p_3 in (f). The circles show the progression of the rupture tip through the centre of the sample. (f): V_P evolution as a function of distance from the rupture tip (circles in (e)) for three points at varying distance perpendicular to the fault plane.

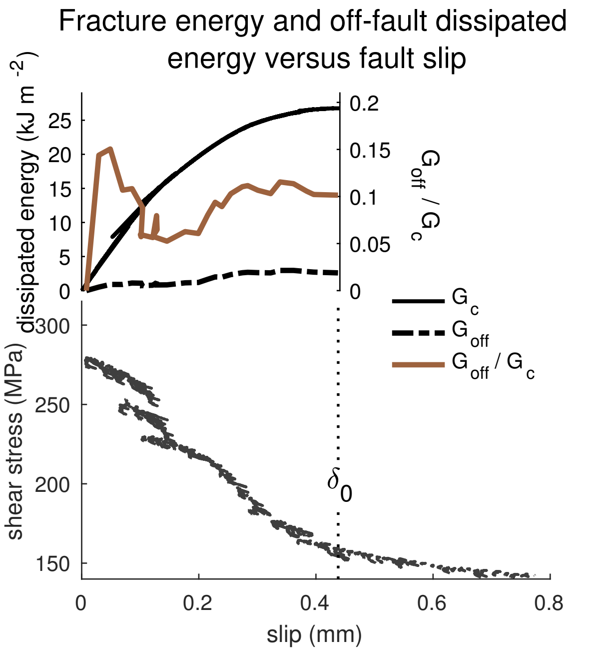

Figure 4: Dissipated energy budget versus fault slip distance. The ratio between the total fracture energy G_c (solid black curve) and the off-fault energy dissipation G_{off} (dashed black curve) shows a large initial off-fault contribution (brown curve). The slip-weakening distance (δ_0) is the interval between onset of rupture and convergence of the shear stress towards the frictional residual strength as shown in the shear stress versus slip plot below. δ_0 is the slip at which the entire fault interface has formed, which is evidenced by the distribution of AE source locations. For the total slip-weakening distance, the relative energy contribution is around 10%.

from mechanical data includes slip along the fault and thus cannot be used to obtain the off-fault strain components necessary to obtain changes in elastic compliance. Instead, the spatial and temporal evolution of the seismic velocity structure is used to obtain these. For each time interval, G_{off} is approximated as

$$G_{off} \approx \frac{1}{2} w \bar{\sigma}_{ij} \Delta S_{ijkl} \bar{\sigma}_{kl}, \quad (1)$$

where $\bar{\sigma}_{ij}$ are the average stress components between two time intervals, ΔS_{ijkl} is the change in the elastic compliance tensor between two time intervals, and w is the width of the damage zone. S_{ijkl} is estimated from the seismic velocities, where we assumed that microcracks were oriented parallel to the loading direction (see text S2). Stress rotations within the damage zone were neglected for simplicity, and for each time interval a single value for ΔS_{ijkl} represented the entire damage zone (see text S2).

A first order approximation of w is established by analysing the spatial extent of permanent damage in our data. Nearly elastic behaviour (i.e., full recovery of V_P) is observed at some distance from the fault interface after passing of the rupture front (point p_3, Fig. 3e and f). This matches qualitatively with the predictions of a stress field around a passing rupture tip [*Freund*, 1990], whereby the stiffness reduction and the full recovery that follows is caused by the rupture tip stress field that dilates or contracts pre-existing flaws. Closer to the fault interface such full recovery is not observed (points p_1 and p_2, Fig. 3f). Within this zone of at most 20 mm in width, permanent microcrack damage is generated. We adopt a more conservative damage zone width w of 10 mm, since the AE source locations are clustered in a more narrow band of 5 to 10 mm around the fault (Fig. 2) [*Zang et al.*, 2000].

G_{off} is around 3 kJ m^{-2} and is a similar order of magnitude to G_{off} established from post-mortem microstructures [*Moore and Lockner*, 1995]. G_{off} is approximately 10% of the fracture energy (Fig. 4), and about 3% of the total dissipated energy during the fracture process. Hence, 90% of G_c is dissipated by on-fault processes. G_{off} accounts for over 15% of G_c for the earliest stage of rupture (up to 0.1 mm of slip, Fig. 4).

5. Discussion

The constraints on rupture energetics were obtained during quasi-static rupture propagation and are representative of the nucleation phase of an earthquake. Once the rupture velocity has accelerated towards the critical wave speed of the rock (equal to the Rayleigh wave speed in in-plane conditions, or to the shear wave speed in anti-plane conditions), the stress field around the rupture tip is distorted relative to that of a quasi-static rupture tip [*Freund*, 1979]. Such a distortion is more likely to increase the size of the off-fault regions where fracturing might occur [*Poliakov et al.*, 2002; *Rice et al.*, 2005]. In addition, the transient rupture tip stress field imposes high strain rates on the off-fault rock volume, which results in increased fragmentation [*Grady*, 1982; *Bhat et al.*, 2012]. G_{off} is thus expected to increase with increasing rupture velocity, changing the ratio G_{off} over total energy dissipation. Therefore, the quasi-static ratio of 3% estimated from our experimental data is a lower bound for dynamic ruptures, but provides a unique calibration benchmark for dynamic rupture models that allow for off-fault damage [*Xu et al.*, 2015; *Thomas and Bhat*, 2018]. Such models predict a maximum drop in V_P of around 30% [*Xu et al.*, 2015; *Thomas and Bhat*, 2018], which is consistent with the maximum drop of 25% observed here.

This maximum drop in V_P of 25% during experimental rupture is of a similar order to geophysical observations on coseismic V_P reduction near recently ruptured faults [*Cochran et al.*, 2009; *Allam and Ben-Zion*, 2012; *Froment et al.*, 2014]. However, these velocity reductions were the product of multiple ruptures with a higher rupture velocity than our experimental rupture, and they also reflect the post-seismic state rather than the co-seismic state that we document here – thus without the transient reduction of elastic properties. Geophysical observations of seismic velocity reductions caused by single rupture events are of the order of 20-45%, but are restricted to S-wave velocity only [*Karabulut and Bouchon*, 2007; *Wu et al.*, 2009]. Rather than directly comparing the absolute values observed here with those measured on faults, our constraints on rupture energetics of laboratory-sized samples can be upscaled to larger faults by relying on scaling relations established by other studies.

First, studies along exhumed faults suggest that damage zone width increases linearly with total fault displacement [*Savage and Brodsky*, 2011; *Faulkner et al.*, 2011], and total fault displacement is linearly proportional to fault length [*Cowie and Scholz*, 1992]. Earthquake fault slip δ increases linearly with fault length [*Scholz*, 1982]. From this it follows that damage zone width scales linearly with fault slip δ [*Savage and Brodsky*, 2011; *Faulkner et al.*, 2011]. G_{off} will increase with increasing damage zone width, assuming that the drop in elastic moduli is independent of δ (i.e. the off-fault drop in elastic moduli occurs only during the slip-weakening phase). This implies that $G_{off} \propto \delta$, and the ratio of G_{off} to total energy dissipation, which is 3% for our experiment, thus remains constant. Field estimates of this ratio are of the order of 1% [*Chester et al.*, 2005; *Rockwell et al.*, 2009], which further supports this conclusion.

Second, seismological estimates and theoretical predictions indicate that fracture energy G_c scales with fault slip δ with an exponent λ [*Viesca and Garagash*, 2015; *Brantut and Viesca*, 2017]. By adopting aforementioned linear scaling of G_{off} with δ, we obtain $G_{off}/G_c \propto \delta^{1-\lambda}$. The exponent $\lambda \approx 2$ for small earthquakes (slip less than around 10 cm, $M_w \lesssim 4$) and $\lambda < 1$ for larger events [*Viesca and Garagash*, 2015; *Brantut and Viesca*, 2017]. Thus, we expect the ratio G_{off}/G_c (for which we measure $G_{off}/G_c \approx 10\%$) to decrease initially with increasing slip and earthquake magnitude, and subsequently to stabilise or slightly increase with earthquake slip and magnitude.

These scaling relations are valid for total fault displacements up to a km, because at larger displacements the extent of the damage zone is not proportional to displacement anymore [*Savage and Brodsky*, 2011], but depends on the width of the fault (which equals the seismogenic depth for strike-slip faults) [*Ampuero and Mao*, 2017; *Scholz*, 2019]. Similarly, there may be a cross-over from δ being proportional to fault length at smaller fault lengths, to δ being proportional to the fault width [*Scholz*, 1994]. In that case, our scaling relations for G_c are valid for larger earthquakes as well.

Our experimental results have been obtained in an initially intact material with a large cohesion, whereas many earthquakes occur along preexisting faults, possibly containing clay-rich gouge. In that case, the fault is likely to have a lower peak strength and a shorter slip weakening distance [*Ohnaka*, 2003], which decreases the size of the rupture tip processes zone and reduces the amount of damage. The off-fault dissipated energy for ruptures along natural faults is thus expected to be lower than for rupture in intact material. In terms of the ratio G_{off}/G_c, a rigorous estimate for natural faults should include the nature of the fault zone material and consider the roughness of faults. Fault roughness affects both G_c [*Ohnaka*, 2003] and G_{off} [*Johri et al.*, 2014], and experiments conducted on initially intact materials (generating a spontaneous fault roughness during fault growth) provide a useful benchmark for more advanced numerical models.

The data presented in this study provide new insight in rupture processes, particularly the strong influence of the transient *in situ* stress state during rupture on the seismic velocities and elastic moduli both inside and outside the fault damage zone (Fig. 2). We infer moduli variations even in the original host rock, due to the presence of pre-existing flaws. The effect of damage on the seismic velocity structure of faults is hence strongly coupled to the local stresses around them. Therefore, observations from structural analysis in terms of fault rock microcracking are not expected to match necessarily the *in situ* elastic moduli distribution (and anisotropy) under realistic crustal stress states.

The damage-induced reduction in elastic moduli around the propagating rupture tip (Fig. 2) suggests local dilatancy of the rock. When pore fluids are present, dilatancy causes a drop in pore fluid pressure that stabilises brittle failure [*Martin III*, 1980]. The pore fluid pressure drop may decrease the efficiency of fluid-driven slip-weakening processes such as thermal pressurisation [*Lachenbruch*, 1980], but its effect can only be assessed fully when the changes in local pore fluid pressure, permeability and storage capacity of the rock near the fault interface are known [*Brantut*, 2019].

A substantial component of the seismic waves radiated from the rupture tip process zone may be caused by off-fault reduction of elastic moduli in addition to radiation from a classic planar rupture [*Ben-Zion and Ampuero*, 2009]. Theoretical first order magnitude estimates of this off-fault component are based on an arbitrary off-fault drop in pre- to post-rupture stiffness of 50%, assuming isotropic elasticity [*Ben-Zion and Ampuero*, 2009]. Here, we verify that the *P*-wave modulus indeed drops by 50%, and we provide the temporal and spatial evolution of the *in situ* stiffness matrix including anisotropy. Thus, our results can help to improve estimates of earthquake source properties, and predictions of strong ground motion caused by seismic radiation.

The laboratory-scale seismic tomography method used here provides a unique constraint on the elastic properties of propagating faults and on the energetics of rupture. We show a significant drop of elastic parameters during the slip weakening phase which may influence mechanisms of slip that follow thereafter, and affects seismic radiation and strong ground motions. The methodology opens new possibilities to quantify the effect of key parameters, such as pressure and fluid flow, on the three dimensional evolution in rock properties under realistic crustal stress conditions.

Acknowledgments. We thank La Générale du Granit for their generosity in providing Lanhélin granite. This work was supported by the UK Natural Environment Research Council, grants NE/K009656/1 to NB and NE/M004716/1 to TMM and NB. FMA, NB, ECD performed the experiment. FMA processed raw data, FMA and NB performed analysis. NB created inversion and AE relocation codes. FMA and NB wrote the paper. All authors discussed the results. FaATSO and the AE relocation code found at http://github.com/nbrantut/faatso.git. All data needed to evaluate the conclusions in the paper are present in the paper and/or the Supplementary Materials. Additional data related to this paper may be found at the NGDC repository of the British Geological Survey.

References

Allam, A., and Y. Ben-Zion, Seismic velocity structures in the southern california plate-boundary environment from double-difference tomography, *Geophysical Journal International*, *190*(2), 1181–1196, 2012.

Ampuero, J.-P., and X. Mao, Upper limit on damage zone thickness controlled by seismogenic depth, in *Fault Zone Dynamic Processes: Evolution of Fault Properties During Seismic Rupture*, edited by M. Thomas, H. Bhat, and T. Mitchell, John Wiley & Sons, 2017.

Ben-Zion, Y., and J.-P. Ampuero, Seismic radiation from regions sustaining material damage, *Geophysical Journal International*, *178*(3), 1351–1356, doi:10.1111/j.1365-246X.2009.04285.x, 2009.

Bhat, H., A. Rosakis, and C. Sammis, A Micromechanics Based Constitutive Model for Brittle Failure at High Strain Rates, *Journal of Applied Mechanics*, *79*, 031,016.1 – 031,016.12, doi:10.1115/1.4005897, 2012.

Brantut, N., Time-resolved tomography using acoustic emissions in the laboratory, and application to sandstone compaction, *Geophysical Journal International*, (February 2018), doi:10.1093/gji/ggy068, 2018.

Brantut, N., Fluid pressure drop and vaporisation during dynamic rupture, *pre-print arXiv:1904.10906v2*, pp. 1–11, 2019.

Brantut, N., and R. C. Viesca, The fracture energy of ruptures driven by flash heating, *Geophysical Research Letters*, doi:10.1002/2017GL074110, 2017.

Chester, J., F. Chester, and A. Kronenberg, Fracture surface energy of the Punchbowl fault, San Andreas system, *Nature*, *437*(7055), 133–136, doi:10.1038/nature03942, 2005.

Cochran, E., Y. Li, P. Shearer, S. Barbot, Y. Fialko, and J. Vidale, Seismic and geodetic evidence for extensive, long-lived fault damage zones, *Geology*, *37*(4), 315–318, doi:10.1130/G25306A.1, 2009.

Cowie, P., and C. Scholz, Physical explanation for the displacement-length relationship of faults using a post-yield fracture mechanics model, *Journal of Structural Geology*, *14*(10), 1133–1148, 1992.

Faulkner, D., T. Mitchell, E. Jensen, and J. Cembrano, Scaling of fault damage zones with displacement and the implications for fault growth processes, *Journal of Geophysical Research*, *116*(B5), B05,403, doi:10.1029/2010JB007788, 2011.

Freund, L., The mechanics of dynamic shear crack propagation, *Journal of Geophysical Research: Solid Earth*, *84*(B5), 2199–2209, doi:10.1029/JB084iB05p02199, 1979.

Freund, L., *Dynamic Fracture Mechanics*, 1–563 pp., Cambridge University Press, Cambridge, 1990.

Froment, B., J. McGuire, R. van der Hilst, P. Gouedard, E. Roland, H. Zhang, and J. Collins, Imaging along-strike variations in mechanical properties of the Gofar transform fault , East Pacific Rise, *Journal of Geophysical Research: Solid Earth*, *119*, 1–20, doi:10.1002/2014JB011270.Received, 2014.

Grady, D., Local inertial effects in dynamic fragmentation, *Journal of Applied Physics*, *53*(1), 322–425, 1982.

Johri, M., E. Dunham, M. Zoback, and Z. Fang, Predicting fault damage zones by modeling dynamic rupture propagation and comparison with field observations, *Journal of Geophysical Research: Solid Earth*, *119*, 1–22, doi:10.1002/2013JB010335.Received, 2014.

Kanamori, H., and L. Rivera, Energy partitioning during an earthquake, *Geophysical Monograph Series*, *170*, 3–13, doi:10.1029/170GM03, 2006.

Karabulut, H., and M. Bouchon, Spatial variability and non-linearity of strong ground motion near a fault, *Geophysical Journal International*, *170*(1), 262–274, doi:10.1111/j.1365-246X.2007.03406.x, 2007.

Lachenbruch, A., Frictional heating, fluid pressure, and the resistance to fault motion., *Journal of Geophysical Research*, *85*(B11), 6097–6112, doi:10.1029/JB085iB11p06097, 1980.

Lockner, D., J. Byerlee, V. Kuksenko, A. Ponomarev, and A. Sidorin, Quasi-static fault growth and shear fracture energy in granite, *Nature*, *350*(6313), 39–42, doi:10.1038/350039a0, 1991.

Lockner, D. A., J. B. Walsh, and J. D. Byerlee, Changes in seismic velocity and attenuation during deformation of granite, *Journal of Geophysical Research*, *82*(33), 5374–5378, 1977.

Martin III, R., Pore pressure stabilization of failure in westerly granite, *Geophysical Research Letters*, *7*(5), 404–406, 1980.

Moore, D., and D. Lockner, The role of microcracking in shear-fracture propagation in granite, *Journal of Structural Geology*, *17*(1), doi:10.1016/0191-8141(94)E0018-T, 1995.

Nielsen, S., E. Spagnuolo, S. Smith, M. Violay, G. Di Toro, and A. Bistacchi, Scaling in natural and laboratory earthquakes, *Geophysical Research Letters*, *43*, 1504–1510, doi:10.1002/2015GL067490.1., 2016.

Ohnaka, M., A constitutive scaling law and a unified comprehension for frictional slip failure, shear fracture of intact rock, and earthquake rupture, *Journal of Geophysical Research*, *108*(B2), 1–21, doi:10.1029/2000JB000123, 2003.

Poliakov, A., R. Dmowska, and J. Rice, Dynamic shear rupture interactions with fault bends and off-axis secondary faulting, *Journal of Geophysical Research: Solid Earth*, *107*(B11), doi:10.1029/2001JB000572, 2002.

Rice, J., C. Sammis, and R. Parsons, Off-Fault Secondary Failure Induced by a Dynamic Slip Pulse, *Bulletin of the Seismological Society of America*, *95*(1), 109–134, doi:10.1785/0120030166, 2005.

Rice, J. R., The mechanics of earthquake rupture, in *Physics of the Earth's Interior*, edited by A. M. Dziewonski and E. Boschi, Proc. Intl. School of Physics E. Fermi, Italian Physical Society/North Holland Publ. Co., 1980.

Rockwell, T., M. Sisk, G. Girty, O. Dor, N. Wechsler, and Y. Ben-Zion, Chemical and physical characteristics of pulverized tejon lookout granite adjacent to the San Andreas and garlock faults: Implications for earthquake physics, *Pure and Applied Geophysics*, *166*(10-11), 1725–1746, doi:10.1007/s00024-009-0514-1, 2009.

Savage, H., and E. Brodsky, Collateral damage: Evolution with displacement of fracture distribution and secondary fault strands in fault damage zones, *Journal of Geophysical Research: Solid Earth*, *116*(3), doi:10.1029/2010JB007665, 2011.

Scholz, C., Scaling laws for large earthquakes: Consequences for physical models, *Bulletin of the Seismological Society of America*, *72*(1), 1982.

Scholz, C., Reply to Comments on "A Reappraisal of Large Earthquake Scaling", *Bulletin of the Seismological Society of America*, *84*(5), 1677–1678, 1994.

Scholz, C., *The Mechanics of Earthquakes and Faulting*, 3rd editio ed., Cambridge University Press, Cambridge, 2019.

Thomas, M., and H. Bhat, Dynamic Evolution Of Off-Fault Medium During An Earthquake : A Micromechanics Based Model, *Geophysical Journal International*, (May), 1–32, doi:10.1093/gji/ggy129, 2018.

Tinti, E., P. Spudich, and M. Cocco, Earthquake fracture energy inferred from kinematic rupture models on extended faults, *Journal of Geophysical Research: Solid Earth*, *110*(12), 1–25, doi:10.1029/2005JB003644, 2005.

Viesca, R., and D. Garagash, Ubiquitous weakening of faults due to thermal pressurization, *Nature Geoscience*, *8*(11), 875–879, doi:10.1038/ngeo2554, 2015.

Wilson, B., T. Dewers, Z. Reches, and J. Brune, Particle size and energetics of gouge from earthquake rupture zones, *Nature*, *434*(7034), 749, 2005.

Wong, T.-F., Shear fracture energy of Westerly granite from post-failure behavior, *Journal of Geophysical Research: Solid Earth*, *87*(B2), 990–1000, doi:10.1029/JB087iB02p00990, 1982.

Wong, T.-F., On the normal stress dependence of the shear fracture energy, in *Earthquake Source Mechanics, Geophys. Monogr. Ser.*, vol. 37, edited by S. Das, J. Boatwright, and C. Scholz, pp. 1–11, American Geophysical Union, Washington, D.C., 1986.

Wu, C., Z. Peng, and Y. Ben-zion, Non-linearity and temporal changes of fault zone site response associated with strong ground motion, *Geophysical Journal International*, *176*(1), 265–278, doi:10.1111/j.1365-246X.2008.04005.x, 2009.

Xu, S., Y. Ben-Zion, J.-P. Ampuero, and V. Lyakhovsky, Dynamic ruptures on a frictional interface with off-fault brittle damage: feedback mechanisms and effects on slip and near-fault motion, *Pure and Applied Geophysics*, *172*(5), 1243–1267, 2015.

Zang, A., F. Wagner, S. Stanchits, C. Janssen, and G. Dresen, Fracture process zone in granite, *Journal of Geophysical Research*, *105*(B10), 23,651–23,661, doi:10.1029/2000JB900239, 2000.

F.M. Aben (f.aben@ucl.ac.uk)

Supporting Information for ”Rupture energetics in crustal rock from laboratory-scale seismic tomography”

Franciscus M. Aben   Nicolas Brantut   Thomas M. Mitchell
Emmanuel C. David
Department of Earth Sciences, University College London
London, UK

July 23, 2019

Contents of this file

1. Text S1 to S2
2. Figures S1 to S5

Additional Supporting Information (Files uploaded separately)

1. Captions for Movie S1

Introduction The supporting information consists of the methodology used to determine the position of the rupture tip through time (text S1), and the detailed equations used to determine the fracture energy G_{c} and the elastic compliances from the tomography (text S2). We present supporting figures that show the anisotropy evolution during rupture (Figure S3) and the post-mortem microstructures (Figure S4). Figure S5 shows a tomographic slice of a ‘failed’ quasi-static rupture experiment performed at the same conditions, and reveals similar features to the presented experiment in the main text. Last, we have included movie S1, which shows the tomography result for each time interval and highlights the propagating rupture (Movie S1).

Text S1. Determination of the rupture tip position

Several studies have obtained 2D[7, 2, 4] and 3D[6] ultrasonic tomography data on deforming rock under laboratory conditions, using active ultrasonic data only. The quasi-Newton inversion algorithm FaATSO[1] used in this study extents laboratory-scale tomography by: i) Using passive source data (acoustic emissions) in addition to active sources to increase ray coverage in the sample volume, ii) computing ultrasonic ray paths rather than assuming straight ones, and iii) the results are obtained under high pressure conditions without compromising the sample setup.

For each time interval, the position of the rupture front was determined from the AE events that occurred within the specified time interval. The AE source locations were relocated by using the 3D seismic velocity structure. A convex hull was then defined around the volume of AE source locations, excluding clusters of three AEs or less that were separated by more than 5 mm from the other AEs. Next, the vertices and edges of this seismically active volume were projected onto a surface with a 45° strike. The dip of this surface (relative to the horizontal) was determined by a linear fit through the AE locations. From the resulting 2D-projection we determined the seismically active portion of the fault plane, the progressive growth of the fault, and the fault angle over time (Fig. S1).

The rupture starts at a 45° degree dip (Fig. S1a) and progressively increases towards a final dip of around 63°. The goodness of fit for the angle (Fig. S1b) gives some insight into the scatter of the AE source locations (i.e. a lower goodness of fit indicates more scatter): it increases as the fault grows, and is highest for the time intervals during frictional sliding. This means that the AE source locations tend to be more concentrated on the fault plane at later stages of rupture, while being more diffuse during the fault growth stage. The seismically active fault surface area stays relatively constant throughout the rupture (Fig. S1c), although time intervals containing more AE events typically show a larger active surface area. There is a significant increase in seismically active area for the time intervals during frictional sliding. Hence, the whole fault surface is seismically active, while during rupture propagation only the zone in the wake of the rupture front is active. For the first stages of rupture, the rupture front progresses mostly on one side of the sample (Fig. S1d). Subsequently, rupture front progression is limited the other side of the sample. The fault angle increases during this rebalancing stage (Fig. S1e). From time interval 15 onward, the rupture front progresses across the whole width of the sample (Fig. S1e).

The final fault plane does not show the increase in angle inferred from the AE source locations. In the area where the fault plane angle was initially low (45°), the fault has been overprinted by the 60° fault surface. This is apparent from the AE source locations during the late rupture stage and the frictional sliding stage.

A similar shift to the final fault plane is visible in the seismic velocity tomography as the early stage low velocity zone migrates upwards in the later stages of rupture. Also, post-mortem microstructures (Fig. S4) show only one well-defined high angle fault plane (60°). Thus, the early fault plane is a region of diffuse microcracking at a 45° angle. Hence, very little slip is accumulated in this early stage and a relatively larger amount of energy is dissipated into off-fault microcracking relative to the later stages of rupture (Fig. 3 main text).

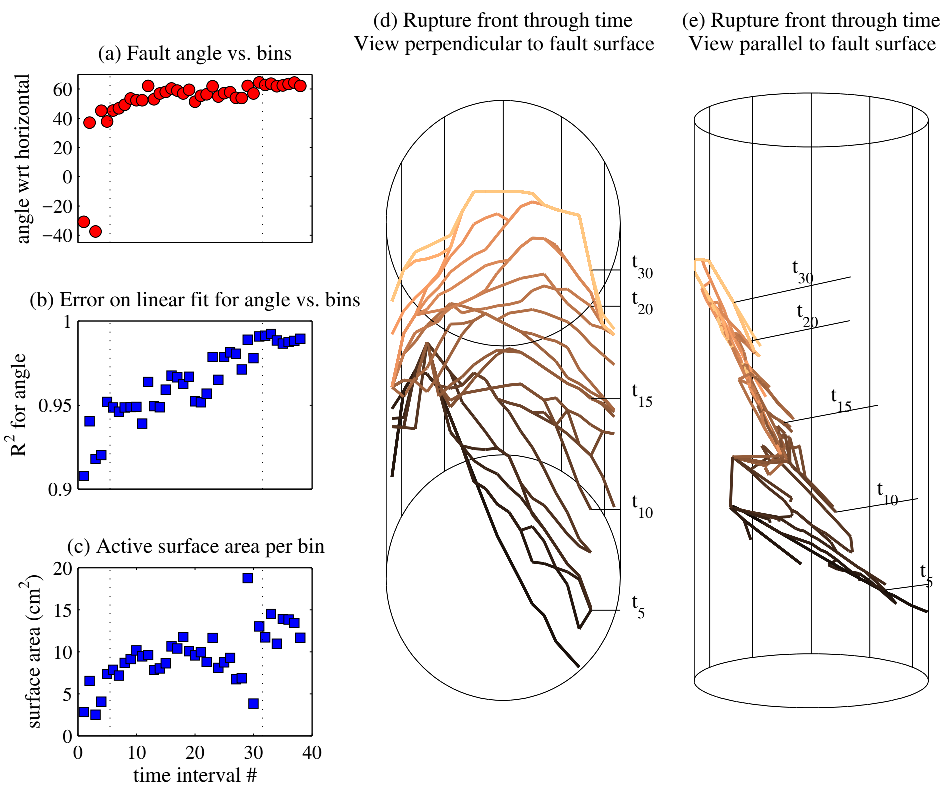

Figure S1: Active fault surface and rupture tip over time (a): Fault angle for each time interval. (b): The R^2 value for determination of the fault angle. (c): Seismically active surface area for each time interval. (a)-(c): The two dashed vertical lines represent the onset of rupture (left line) and the onset of frictional sliding (right line). (d): Rupture front progressing through time. Some of the time intervals are indicated on the right. View perpendicular to fault surface. (e): Rupture front progressing through time, view parallel to fault surface.

Text S2. Calculation of fracture energy and off-fault energy dissipation

Fracture energy

The total fracture energy G_c spend on propagating the fault was obtained following the approach of Wong. First, the unloading loops were removed from the stress and strain data so that only mechanical data associated to loading remained. The shear stress on the fault plane was calculated from the axial stress, assuming a fault dip of 60°. The axial shortening was corrected for elastic strain by using the intact elastic moduli of the rock. The onset of localisation was set at the point where the linear relation between inelastic axial shortening versus radial strain broke down, which roughly correlates to the peak stress. We assume that from the localisation onward all permanent axial shortening measured by the LVDTs is due to slip along the fault. This allows us to calculate the slip history of the fault plane at a 60° angle from the axial strain data. G_c is equal to the area bounded by the shear stress - fault slip curve, down to the frictional strength of the fault at 155 MPa shear stress. G_c equals about 2.7×10^4 Jm^{-2}.

Off-fault energy dissipation

Next, we calculated the amount of energy needed to soften the rock in the damage zone. Here we assume that the increase in elastic compliance is caused by the presence of cracks. The energy required to increase the elastic compliance, equal the off-fault energy dissipation G_off, is the change in elastic stored strain energy:

$$G_\mathrm{off} = \frac{1}{2} w \, \Delta\varepsilon_{ij}\sigma_{ij}, \tag{1}$$

where σ_{ij} are the macroscopic stress components, $\Delta\varepsilon_{ij}$ is the variation of elastic strain, and w the width of the damage zone. The summation convention for repeated indices is used here. The variation of elastic strain is derived from the variation of the compliance tensor, ΔS_{ijkl}, as:

$$\Delta\varepsilon_{ij} = \Delta S_{ijkl}\sigma_{kl}, \tag{2}$$

so that (1) becomes:

$$G_\mathrm{off} = \frac{1}{2} w \, \sigma_{ij}\Delta S_{ijkl}\sigma_{kl} = \frac{1}{2} w \, \sigma_{ij}\Delta C^{-1}_{ijkl}\sigma_{kl}, \tag{3}$$

where $\Delta C = \Delta S^{-1}$ denotes the stiffness tensor.

To apply equation (3) we simplified the results of the seismic tomography by defining a zone of width w around the fault where elastic properties are allowed

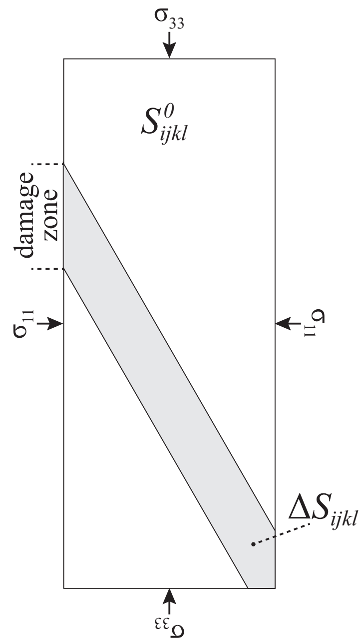

Figure S2: Setup to calculate the off-fault dissipated energy. The low velocity zone around the fault obtained from the seismic inversion is simplified into a damage zone with reduced elastic properties surrounded by host rock with constant elastic properties of the intact rock.

to change (Fig. S2). The surrounding host rock remains intact (S^0_{ijkl} components are constants). The largest stress component is σ_{33}, σ_{11} is equal to the confining pressure. Although elastic heterogeneities cause rotation of stress within the damage zone[3], we set the stress state within the damage zone equal to the far-field applied σ_{11} and σ_{33} for simplicity.

The measured strain during the experiment is the sum of elastic strain (or strain induced by microcracks) and inelastic slip along the fault. As the inelastic slip is an undesired component in the strain tensor, S_{ijkl} components are calculated from the seismic velocities in the damage zone. Based on microstructural observations, we assume that the reduction of the seismic velocities and the stiffness in the damage zone are caused by the formation of microfractures aligned predominantly with the largest stress component (Fig. S4). Hence, we assume that no microfractures are aligned perpendicular to the highest stress component, and that the damage zone is transversely isotropic. The microfracture density and orientations can be quantified as a crack density tensor α [5]. Tensor α is only valid when we assume no interaction between fractures; i.e., the cracks are randomly positioned [5].

Three components of the stiffness tensor C_{ijkl} can be calculated directly from the horizontal velocity V_P^{h} and vertical velocity V_P^{v} of the damage zone:

$$C_{1111} = C_{2222} = \rho (V_P^{\mathrm{h}})^2 \qquad C_{3333} = \rho (V_P^{\mathrm{v}})^2, \tag{4}$$

where ρ is the density of the granite. The other components of C_{ijkl} are obtained by relating the components of the crack density tensor α_{ij} (the indices indicate the direction to the normal of the cracks) to V_P^{h} and V_P^{v}. Following the assumptions above, $\alpha_{33} = 0$. From equations (22) and (23) in *Sayers and Kachanov* [5], it follows that C_{1111} is a function of α_{11}:

$$C_{1111} = \frac{1}{2}\left[\frac{1}{S^0_{1111} - S^0_{1122} + \alpha_{11}} + \frac{S^0_{1111}}{(S^0_{1111})^2 + S^0_{1111}S^0_{1122} + S^0_{1111}\alpha_{11} - 2(S^0_{1122})^2}\right], \tag{5}$$

with

$$S^0_{1111} = \frac{1}{E_0} \qquad \text{and} \qquad S^0_{1122} = \frac{-\nu_0}{E_0}, \tag{6}$$

where E_0 and ν_0 are the Young's modulus and Poisson's ratio of the intact rock, respectively. α_{11} is thus obtained by inverting equation (5) as:

$$\alpha_{11} = \frac{-4C_{1111}\left[(S^0_{1111})^2 - (S^0_{1122})^2)\right] + \sqrt{D}}{4C_{1111}S^0_{1111}}, \tag{7}$$

with

$$D = \left(-4C_{1111}\left[(S^0_{1111})^2 - (S^0_{1122})^2)\right]\right)^2 - 8C_{1111}S^0_{1111}\left(2C_{1111}\left[(S^0_{1111})^3 + 2(S^0_{1122})^3 - 3S^0_{1111}(S^0_{1122})^2\right] - 2(S^0_{1111})^2 + 2(S^0_{1122})^2\right). \tag{8}$$

Alternatively, α_{11} can be obtained from C_{3333}. However, α_{11} has a greater effect on V_P^{h}, and can thus be established more accurately through C_{1111}. With α_{11} known and by using equations (22)-(27) in *Sayers and Kachanov* [5], the remaining components C_{ijkl} are obtained. The independent components of the compliance tensor S_{ijkl} are given by:

$$S_{1111} = \frac{1}{F}\left(C_{1111}C_{3333} - C^2_{1133}\right), \tag{9}$$

$$S_{1122} = \frac{1}{F}\left(C^2_{1133} - C_{1122}C_{3333}\right), \tag{10}$$

$$S_{1133} = \frac{1}{F}\left(C_{1133}(C_{1111} - C_{1122})\right), \tag{11}$$

$$S_{3333} = \frac{1}{F}\left(C_{1111}^2 - C_{1122}^2\right), \tag{12}$$

$$S_{4444} = C_{4444}, \tag{13}$$

$$S_{6666} = \frac{2}{C_{1111} - C_{1122}}, \tag{14}$$

with

$$F = (C_{1111} - C_{1122})\left[(C_{1111} + C_{1122})C_{3333} - 2C_{1133}^2\right]. \tag{15}$$

To obtain all the components of S_{ijkl}, we took the minimum V_P^{h} from the seismic tomography at each time interval, with the corresponding V_P^{v} obtained from the V_P^{h} and anisotropy, and applied them to equations (4)-(15). Equation (3) was then used to obtain the off-fault dissipated energy G_{off} for each successive time interval. Shear stress components were not computed and were set to zero, so that equation (3) becomes:

$$\begin{aligned} G_{\mathrm{off}} = {} & \frac{1}{2} w\, \bar{\sigma}_{33}\left(2\bar{\sigma}_{11}\Delta S_{1133} + \bar{\sigma}_{33}S_{3333}\right) \\ & + w\, \bar{\sigma}_{11}\left(\bar{\sigma}_{11}(S_{1122} + S_{1111}) + \bar{\sigma}_{33}S_{1133}\right). \end{aligned} \tag{16}$$

The cumulative off-fault dissipated energy is the sum of the energies obtained for the individual time intervals.

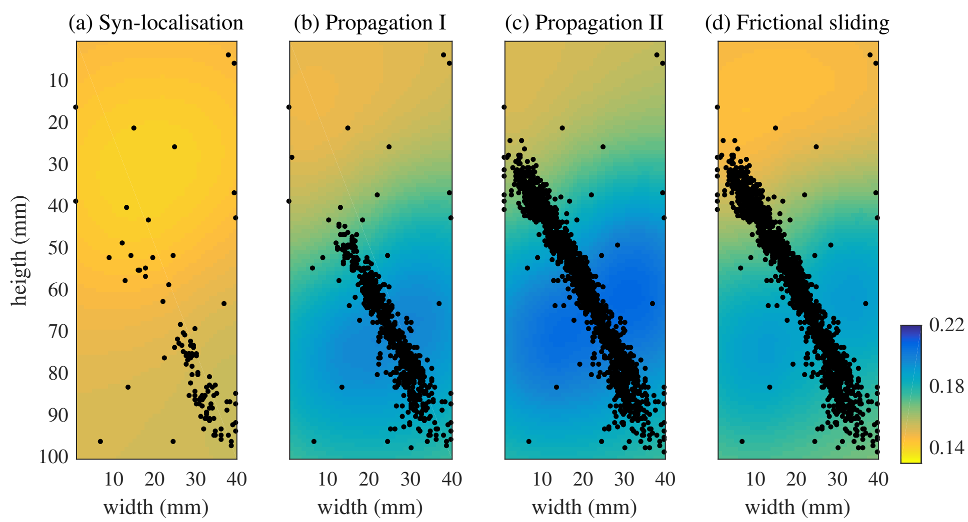

Figure S3: *P*-wave anisotropy structure. (a)-(d) represent the same time intervals as shown in Fig. 1. P-wave anisotropy ranges from 13% initially up to 20% during the propagation of the rupture. The anisotropy decreases when the fault has formed across the sample.

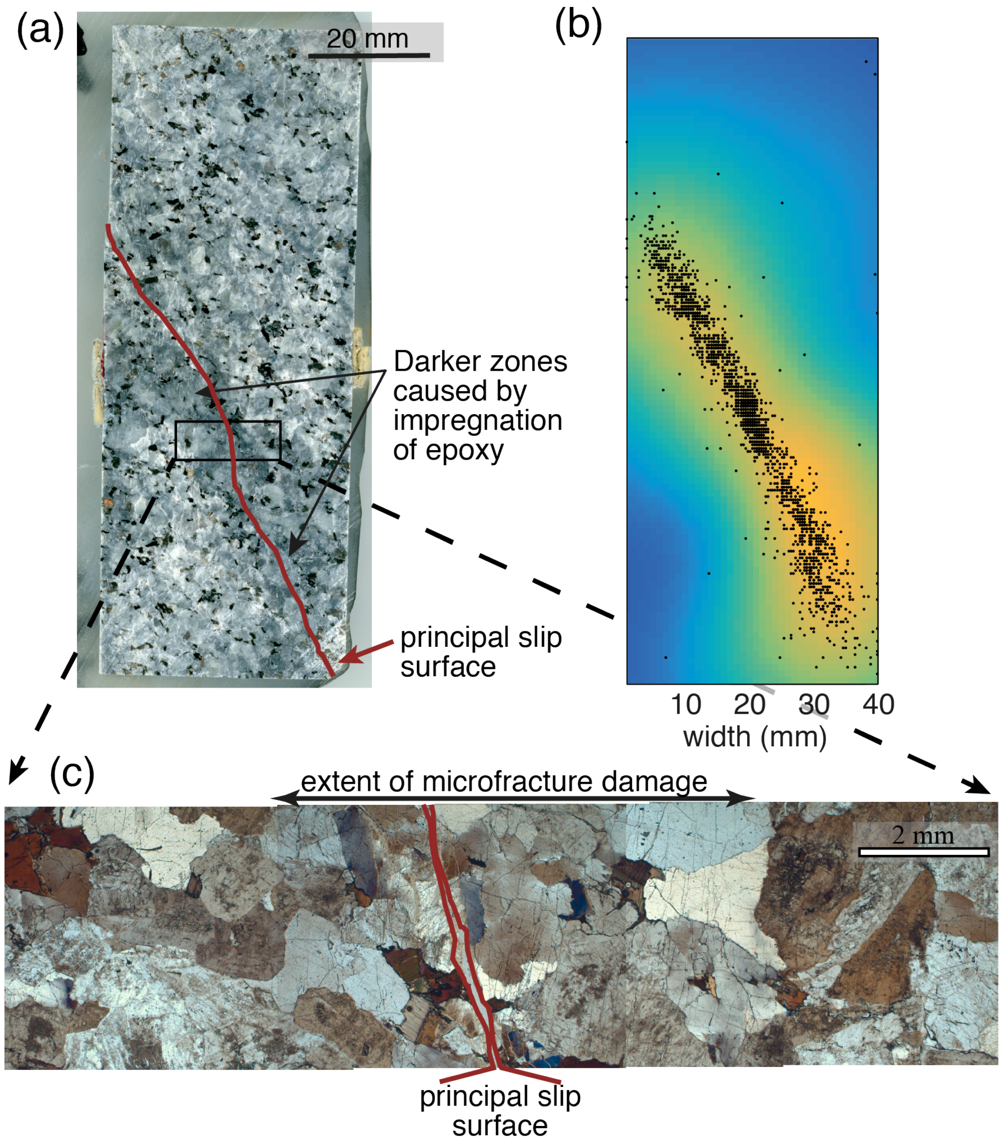

Figure S4: Post-mortem microstructures. (a): Image of a polished section through the center of the sample, perpendicular to the fault. Darker zones around the fault are caused by epoxy impregnating the rock, thus providing a first order estimate of fracture damage. (b): Tomographic slice D from Figure 1 shows that the low velocity zone is at roughly the same location as the dark zones impregnated by epoxy in (a). (c): Microphotographs showing that a zone of microfracture damage extends several millimeters from the fault. Most microfractures are oriented (sub-) vertical. The images were taken with transmitted light and cross polarizers at 45° angle.

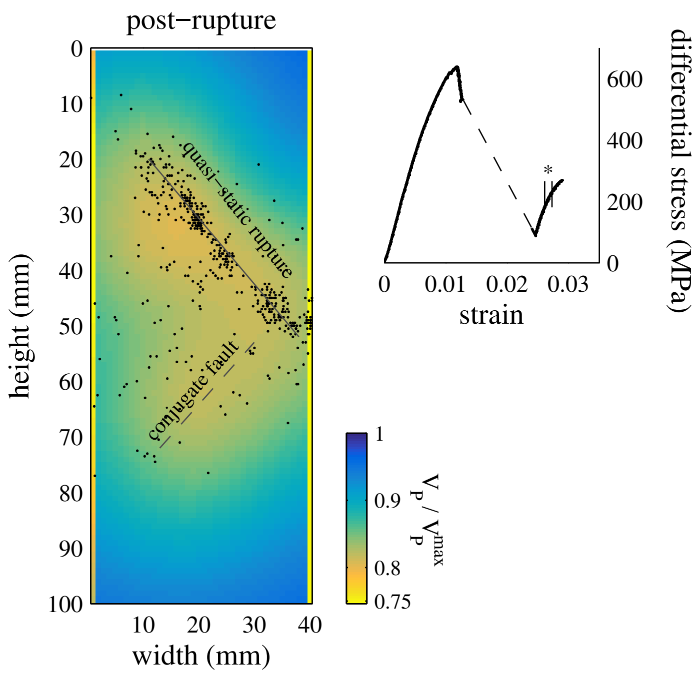

Figure S5: Tomographic slice of the horizontal *P*-wave velocity normalised by the initial velocity, obtained on a sample of Lanhélin granite subjected to quasi-static rupture at 100 MPa confining pressure (i.e. similar conditions to the experiment presented in the main text). The slice runs through the centre of the sample, perpendicular to the rupture. The rupture became unstable and propagated dynamically around 520 MPa differential stress (see stress-strain curve on the right). The tomographic slice corresponds to the stress-strain interval highlighted by the asterisk, and thus reveals the post-failure tomographic structure. AE source locations up to the time interval are projected onto the slice, illustrating the extent of quasi-static rupture propagation. The AE source locations are within 2.5 mm distance perpendicular to the slide, and were determined using the 3D seismic velocity model. The seismic velocities are smoothed to a 1 mm resolution. A nascent conjugate failure plane is highlighted on the tomographic slice, this failure plane did not accumulate any slip and did not develop to a full fault interface. The spatial extent of the low velocity zone and the *P*-wave drop in the low velocity zone of this ‘failed’ quasi-static rupture experiment are of similar of magnitude to the post-rupture *P*-wave structure obtained on the quasi-static rupture shown in Fig. 1d).

Movie S1. Movie of the evolution of the seismic velocities during the controlled rupture experiment. The interval on the stress-strain curve represented by the tomographic slice is highlighted in black. The tomographic slice is oriented similar to the images in Figure 1 in the main text.

References

[1] Brantut, N., Time-resolved tomography using acoustic emissions in the laboratory, and application to sandstone compaction, *Geophys. J. Int.*, *213*, 2177–2192, 2018.

[2] Falls, S. D., R. P. Young, S. R. Carlson, and T. Chow, Ultrasonic tomography and acoustic emission in hydraulically fractured Lac du Bonnet grey granite, *J. Geophys. Res.*, *97*(B5), 6867–6884, 1992.

[3] Faulkner, D. R., T. M. Mitchell, D. Healy, and M. J. Heap, Slip on 'weak' faults by the rotation of regional stress in the fracture damage zone, *Nature*, *444*, 922–925, doi:10.1038/nature05353, 2006.

[4] Jansen, D. P., S. R. Carlson, R. P. Young, and D. A. Hutchins, Ultrasonic imaging and acoustic emission monitoring of thermally induced microcracks in Lac du Bonnet granite, *J. Geophys. Res.*, *98*(B12), 22,231–22,243, 1993.

[5] Sayers, C., and M. Kachanov, Microcrack-induced elastic wave anisotropy of brittle rocks, *J. Geophys. Res.*, *100*(B3), 4149–4156, 1995.

[6] Tudisco, E., P. Roux, S. Hall, and G. Viggiani, Timelapse ultrasonic tomography for measuring damage localization in geomechanics laboratory tests, *J. Acoust. Soc. Am.*, *137*(3), 1389–1400, 2015.

[7] Yukutake, H., Fracturing process of granite inferred from measurements of spatial and temporal variations in velocity during triaxial deformations, *J. Geophys. Res.*, *94*(B11), 15,639–15,651, 1989.